doi:10.20944/preprints202208.0506.v1

Technical Note

A New Data Processing Pipeline for Generating Sea Ice Surface Roughness Products from the Multi-angle Imaging SpectroRadiometer (MISR) Imagery

Ehsan Mosadegh [1],* and Anne W. Nolin [2]

[1] Atmospheric Sciences Graduate Program, University of Nevada, Reno, NV 89557, USA.; emosadegh@nevada.unr.edu
[2] Department of Geography, University of Nevada, Reno, NV 89557, USA; anolin@unr.edu
* Correspondence: emosadegh@nevada.unr.edu

Abstract: Sea ice roughness can serve as a proxy for other sea ice characteristics such as ice thickness and ice age. Arctic-wide maps that represent spatial patterns of sea ice roughness can be used to better characterize spatial patterns of ice convergence and divergence processes. Sea ice surface roughness can also control and quantify turbulent exchange between sea ice surface and atmosphere and therefore influence surface energy balance at the basin scale. We have developed a data processing system that produces georeferenced sea ice roughness rasters that can be mosaicked to produce Arctic-wide maps of sea ice roughness. This approach starts with Top-of-Atmosphere radiance data from the Multi-angle Imaging SpectroRadiometer (MISR). We used red-band angular data from three MISR cameras (Ca, Cf, An). We created a training data set in which MISR pixels were matched with co-located and concurrent lidar-derived roughness measurements from the Airborne Topographic Mapper (ATM). We used a K-nearest neighbor algorithm with the training data to calibrate the multi-angle data to values of surface roughness and then applied the algorithm to Arctic-wide MISR data for two 16-day periods in April (spring) and July (summer). After georeferencing the roughness rasters, we then mosaicked each 16-day roughness dataset to produce Arctic-wide maps of sea ice roughness for spring and summer. Assessment of the results shows good agreement with independent ATM roughness data, not used in model development. A preliminary exploration of spatial and seasonal changes in sea ice roughness for two locations shows the ability to characterize the roughness of different ice types and the results align with previous studies. This processing system and its data products can help the sea ice research community to gain insights into the seasonal and interannual changes in sea ice roughness over the Arctic.

Keywords: sea ice; surface roughness; remote sensing; MISR

1. Introduction

The Arctic is warming faster than any region on the planet [1] and sea ice is highly sensitive to this rapid climate change [2-7], and it has been rapidly declining over the past three decades in the Arctic region [8-10]. Since 1962, spaceborne sensors have mapped sea ice characteristics and have served as a valuable resource for understanding changes in the Arctic cryosphere [11-15]. In situ and airborne data acquisitions are challenging in the polar regions due to difficulties in accessing such a vast and extreme environment. Thus, satellite remote sensing has become a valuable technique for performing Arctic-wide spatio-temporal analysis, especially mapping sea ice characteristics. Satellite remote sensing techniques have been used in numerous studies to retrieve and map properties of sea ice over the Arctic [16-20]. These techniques provide Arctic researchers with sea ice characteristics such as ice age, extent, albedo, thickness, motion, and roughness. Sea ice surface roughness influences synthetic aperture radar and scatterometer retrievals of sea ice type [21], but few studies have explicitly and quantitatively mapped the roughness of sea ice on an Arctic-wide basis [16], [19].

Dynamics and thermodynamic processes impact and modulate properties of sea ice such as ice thickness, ice age, ice extent, melt pond extent, and surface roughness. These properties consequently influence the surface energy balance and planetary boundary layer processes such as turbulent fluxes of momentum (drag) and sensible/latent heat over the ice surface [22-25]. Sea ice surface roughness establishes the linkage with atmospheric processes through boundary layer turbulence [23], [24], [26]. Sea ice surface roughness topography has spatial and temporal variations and this will reflect in spatial and temporal patterns of other sea ice parameters such as aerodynamic roughness length and drag coefficients [24], [27], and these parameters are needed to estimate wind stress and boundary layer processes in climate and atmospheric numerical models [25], [28-30]. Sea ice surface roughness affects how surface meltwater spread across the surface. Melt ponds on smooth ice can aggregate and spread across a larger area, which consequently, decreases sea ice surface albedo. [19], [31-36].

Surface roughness is the variation in surface topography and is defined as the root mean squared deviations of measured surface elevations from a flat reference surface [37]. Sea ice surface roughness is a key property that, although not produced as a standard remote sensing data product, has been mapped and quantified using data from the Multi-angle Imaging SpectroRadiometer (MISR) [37], [38]. One of the main advantages of MISR data is its simultaneous multiangular reflectance information that creates a link between structural characteristics (e.g., surface roughness) and radiative quantities of a scene [39]. These structural characteristics will give rise to angular reflectance patterns that are independent of spectral reflectance patterns. For instance, when mapping surface roughness, it is the angular signature that provides information, rather than the more widely used spectral signature [38], [40]. Nolin et al. (2002) demonstrated that MISR multiangular reflectance data can be used to characterize sea ice surface roughness. They defined a qualitative proxy named Normalized Difference Angular Index (NDAI) by combining imagery data from three MISR cameras. Nolin and Mar (2019) demonstrated that sea ice angular signatures can be calibrated using airborne lidar-derived measurements of surface roughness and has the potential to create quantitative maps of sea ice surface roughness. They developed an empirical relationship between multiangular reflectance data from MISR images and sea ice surface roughness measurements from the Airborne Topographic Mapper (ATM) field campaigns over the arctic. They employed and developed a weighted nearest neighbor algorithm to derive estimates of roughness values for newly acquired MISR data samples. Their study demonstrated that the proposed method can characterize and quantify sea ice physical roughness and has the potential for creating maps of surface roughness over the whole Arctic by using MISR multiangular reflectance data.

The overarching goal of this research is to develop and implement a new and efficient data processing pipeline that can be used to create roughness maps of sea ice over the entire Arctic. To achieve this goal, we have developed a detailed methodology that

a) converts large amounts of MISR multiangular information into sea ice roughness images, and;
b) employs a new algorithm that converts the roughness images into geolocated and mosaicked maps of surface roughness over the entire Arctic.

This work supplies the necessary data processing system to analyze the large volume of MISR image data and will lead to a deeper understanding of sea ice roughness over the Arctic.

2. Materials and Methods

Our approach builds on the previous work of Nolin and Mar (2019), using a combination of multiangular reflectance data and airborne lidar data to build, calibrate, and validate a surface roughness data model. What is innovative about this work is that we have created a data processing pipeline that will allow the user to

Preprints (www.preprints.org) | NOT PEER-REVIEWED | Posted: 30 August 2022 doi:10.20944/preprints202208.0506.v1

process massive amounts of image data to create seamless, Arctic-wide mosaics of sea ice surface roughness.

For this research, we used a subset of MISR images for two 16-day periods to extend and assess the performance and application of the sea ice roughness modeling approach and the processing pipeline. Our study area is the Arctic region, north of 60°N latitude. The time frame covers 16 days in April (spring) and 16 days in July (summer) 2016. April corresponds to the approximate annual peak of sea ice extent and July is approximately the time of melt onset (Landy et al., 2015). We wanted to explore the capacity of our method for capturing the seasonal changes in sea ice roughness between spring and summer. The periods are 16 days because that is the exact orbital repeat time for MISR, over which the instrument images nearly the entire globe [41].

2.1 Description of Data Sets

2.1.1 Airborne Topographic Mapper

The Airborne Topographic Mapper (ATM) is a conically-scanning airborne lidar that measures the surface topography of a swath of terrain directly beneath the path of the aircraft [42]. The ATM instrument has been flown onboard the NASA P-3 and DC8 aircraft as part of NASA’s IceBridge campaigns [42]. The instrument flies at a nominal altitude of 500–750 m and uses a scanner angle of 22◦ with a laser footprint of around 1 m, horizontal accuracy of 0.74 m, and vertical precision of 3 cm. Also, elevation accuracy determined by [43] was found to be typically better than 7 cm.

In the ATM ICESSN sea ice roughness data product available from the National Snow and Ice Data Center (NSIDC), and here as well, we used the surface roughness attribute of sea ice which is different from aerodynamic roughness length. Surface roughness is defined as the root mean square (RMS) of deviation of measured surface elevations from a fitted plane with a specific extent [42]. In this data product, the extent is an 80 m “platelet” from an ATM lidar instrument. Post-processing converts the lidar elevations to surface roughness data. Here, we used ATM ICESSN-processed data that were resampled from the initial high-volume elevation data set by fitting overlapping "platelets" of about 80 m in diameter along the flight line using along-track and cross-track slopes. The average and root mean square (RMS) deviation of all elevation points within each platelet are computed to yield values for average elevation and roughness, respectively. We only used the roughness values from the ATM's nadir (zero degrees) scan angle. In the Arctic, ATM-derived sea ice roughness data were collected over the years 2009 - 2019 typically for the months of March, April, and May. Arctic ATM overflights have covered a wide range of sea ice types, including first-year and multi-year ice types.

2.1.2 Multi-angle Imaging SpectroRadiometer (MISR)

MISR is an instrument on the Terra satellite launched by NASA on 18 December 1999. It has nine cameras and each of these cameras views the Earth at a different angle and in four spectral bands. Each camera measures the radiances that are reflected from the Earth's surface to space in a specified direction. MISR uses a Space-Oblique Mercator (SOM) projection/gridding scheme that follows the orbital path of the instrument and preserves the geometry of the multiangular data. There are 233 geographically distinct MISR orbital paths that provide near-global coverage. The 233 paths repeat every 16 days. Each path is subdivided into 180 blocks, with the block numbers increasing from the north to the south pole. Our study area is covered by MISR blocks 1-46. MISR has four spectral bands (blue, green, red, and near-infrared) at each of its nine cameras. The nadir camera has all four bands at a spatial resolution of 275 m while for the non-nadir cameras, only the red band is at 275-m resolution; the other bands are spatially aggregated to 1.1. km resolution [39]. Because roughness can be characterized with multiangular data and since we wish to map roughness at 275-m spatial resolution, we used only the red bands. We used the MISR ML1B2-Ellipsoid data product in this research which includes top of atmosphere (TOA) radiance measurements. MISR data were obtained from the NASA Langley Research Center Atmospheric Science Data Center (ASDC). As with Nolin and Mar (2019), we only used red band radiance information from three MISR cameras (An, Ca, Cf). At high latitudes, the orbits have some spatial overlap. Thus, MISR observes much of the Arctic every two days. Within each image, data from all nine angles are acquired within a seven-minute window.

2.2 Data Preparation and Processing Steps

We began with downloading concurrent and co-located ATM and MISR data. ATM ICESSN roughness data [42] were downloaded from the National Snow and Ice Data Center. MISR Level 1B2 top-of-atmosphere (TOA) radiance data (ML1B2E) were downloaded from the Langley Atmospheric Science Research Center. As previously mentioned the ML1B2E data are in Space Oblique Mercator Projection (SOM) and each 16-day orbital repeat period has 233 paths; each path is composed of 180 blocks. Blocks are spatially offset to accommodate the curvature of each path. We note that standard HDF-EOS processing routines do not assemble the blocks into smoothly contiguous images. In the next step, we converted TOA radiance to TOA reflectance. Reflectance characterizes the roughness of a surface independent of the magnitude of solar illumination. Each MISR HDF file includes all the blocks in a single MISR path which nominally include 180 blocks. Therefore, we then extracted the number of blocks that cover our study area (blocks 1-46). We then applied a land mask to each block of the MISR data to exclude land areas.

For developing and calibrating our training data set we used sea ice roughness data from ATM measurements. Based on the location information and time of each ATM sample we identified MISR pixels that were co-located and concurrent with each ATM measurement. We then assigned each MISR pixel a roughness value based on the average of ATM roughness values within the pixel. We subset the training data set using only those MISR pixels that had 10 or more ATM measurements. After applying this criterion, the final training data set included approximately 11,000 samples for April and 2,200 samples for July. The ATM roughness values allocated to each MISR pixel are the label information for our training data set.

In the prediction step, we used an independent test dataset to predict sea ice surface roughness. These data were not used in building our data model. We developed and tested three models namely simple linear regression (SLR), polynomial linear regression (PLR), and K-nearest neighbor (KNN). For each month (April and July 2016), statistical metrics such as Root Mean Square Error (RMSE), Mean Absolute Error (MAE), Mean Bias Error (MBE), and Coefficient of Determination (R^2) were computed for model assessment. Also, statistical visual tests such as frequency histograms and Q-Q plots were used to evaluate error distributions for each month. Based on these metrics, we selected the KNN algorithm, similar to that used by Nolin and Mar (2019). The original model ran on a single CPU core and was not optimized for big data sets and high-performance computing (HPC) clusters. Processing each input to the data model takes approximately 20 seconds to process a single MISR block on a Linux machine with Intel(R) Xeon(R) CPU E5-2683 v4 processors. Thus, serial processing would take an excessively long time to produce output roughness files. In this data pipeline, we parallelized the main processing algorithm for HPC clusters. The new algorithm can now run on multiple CPU cores. The input files consist of three land-masked TOA reflectance data files about 8 MB each. Each output file contains the estimated sea ice roughness data and is in a generic raw binary file format with a ".dat" file extension. One output data file covers a single MISR Path/Block combination (e.g., roughness_toa_refl_P233_O087029_B024.dat) with 512 by 1024 pixels and is approximately 24 MB in size.

Georeferenced image data are crucial for creating daily sea ice roughness mosaics. To create a georeferenced, map-projected, multi-band raster from the raw data, we need to have the geo-transformation information for each image. Geo-transformation is an affine transformation with 6 parameters that creates a relationship between the image coordinate space and the georeferenced coordinate space. However, we do not have geo-transformation information for each block which is a challenge for producing a georeferenced raster image from an array of roughness data. On the other hand, MISR L1B2 data files are supplied in one single large HDF file which includes all blocks in a single MISR path, and the only georeferenced information in that file is the location of the top left corner of the first block. Therefore, the first and crucial step for mosaicking the roughness data is to create a georeferenced GeoTIFF image from each roughness file.

We developed an algorithm to transform a roughness array into a raster image and added location information to each pixel in the raster. This algorithm calculates the geographic coordinates of a pixel in the output roughness file from its image coordinates using MISRToolkit (MTK) library functions. Then, we used the ground control point (GCP) method to embed the geographic information of each roughness pixel to a multi-band georeferenced GeoTIFF raster. We formed GCPs by selecting 85 pixels from each MISR block. This method matches each pixel in the MISR image frame with its corresponding geographical location in a coordinate frame. We used the MTK and Geospatial Data Abstraction Library (GDAL) Python libraries to develop this algorithm. MTK is a program library that has been developed by JPL for processing MISR datasets. It is a simplified programming interface to access MISR L1B2, L2, conventional, and ancillary data products. GDAL is a software library for reading and writing raster and vector geospatial data formats. In all the mentioned processing steps, we used the MTK C and Python libraries and the GDAL Python library to process MISR data files. To create a mosaic from a large data set of produced georeferenced images, we built our mosaicking algorithm by using the GDAL python library and then created maps of sea ice roughness for the whole Arctic. For producing each map, we processed and merged approximately 9000 roughness files. When multiple pixels overlapped, the mosaicking algorithm computed and stored their average in the mosaic. The general steps we described in the data processing section are visualized in Figure 1.

To evaluate the performance of our method, we compared an independent test data set of ATM data samples with their co-located MISR-estimated sea ice roughness values. This subset of ATM data was not used in the building step of our model and was kept aside for model evaluation. We selected this subset from both April and July 2016 data sets, and we calculated statistics from this comparison. Finally, we inspected two arbitrary locations and visually compared our MISR-derived roughness maps with Landsat 8 and Sentinel-1 images to visually evaluate the accuracy of our MISR-derived surface roughness maps.

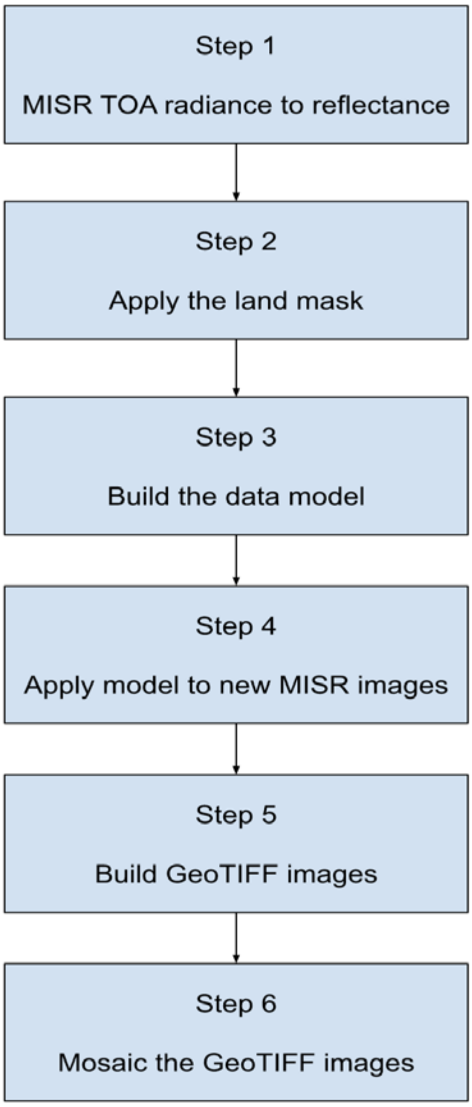

Figure 1. Data processing steps

1. Results

3.1. Evaluating Model Performance

In the process of labeling MISR images with co-located ATM measurements of sea ice roughness and building the training dataset for our model, we found out that the available number of co-located ATM samples per each MISR image pixel is an important factor in the accuracy of the model predictions. After testing several thresholds for the number of ATM samples per pixel, we concluded that the threshold of at least 10 ATM samples per MISR pixel better represents the surface roughness of sea ice in each MISR image pixel for building our model for this study. Also, we restricted the selection of MISR images to the same day that ATM data were acquired. Therefore, in the process of selecting and subsetting MISR images, we only considered MISR images that were acquired on the same day that ATM measurements were also obtained. We finally developed our model data set based on at least a 10-ATM-samples-per-MISR-pixel threshold on the same day of MISR-ATM overpass over a region and then used our developed model to estimate sea ice roughness for both April and July 2016 to estimate the condition of sea ice roughness for the spring and summer seasons, respectively.

We compared the performance of our KNN model with two other standard parametric regression models: the simple linear regression (SLR) model and the

doi:10.20944/preprints202208.0506.v1

polynomial linear regression (PLR) model. To evaluate the performance of the KNN model with these other regression models, we calculated and compared several statistical measures including R^2, RMSE, MAE, MBE, and NSE as our performance metrics among all 3 candidate models. Table 1 presents the performance metrics for both the training and the independent test dataset for the 16 days in April and July 2016. The performance of the developed model is usually evaluated based on its skill on the independent test dataset because this dataset is not used in training the model and therefore this score may be more representative of the true skill of the trained model. A comparison of performance metrics for the independent test dataset in Table 1 illustrates that KNN is the best model for both April and July. For instance, KNN has the highest R^2 for both April and July among all three models. Also, RMSE and MAE bias metrics for April and July on the independent test dataset have lower values compared to two other models for each month. MBE shows the bias of a model and a negative value shows that a model underestimates the modeled roughness. MBE of our modeling results indicates that all three models underestimate roughness. KNN for July has the lowest bias (-0.09 cm) and the highest bias (-0.16 cm) for April, but both bias values are negligible. Because the results of the NSE test metric were similar to R^2, we did not include the NSE metric results in this table. Figure 1 shows the R^2 plots for the corresponding values in Table 1.

Table 1. Statistics of model performance.

	R2		RMSE (cm)		MAE (cm)		MBE (cm)	
SimpleLinearRegr	training	test	training	test	training	test	training	test
April	0.12	0.13	6.49	6.44	4.99	4.93	0	-0.12
July	0.06	0.05	5	4.9	3.7	3.6	0	-0.14

	R2		RMSE (cm)		MAE (cm)		MBE (cm)	
PolyLinearRegr	training	test	training	test	training	test	training	test
April	0.28	0.29	5.87	5.8	4.45	4.36	0	-0.15
July	0.11	0.09	4.77	4.84	3.56	3.6	0	-0.09

	R2		RMSE (cm)		MAE (cm)		MBE (cm)	
KNN	training	test	training	test	training	test	training	test
April	0.66	0.5	4.05	4.91	2.81	3.39	-0.08	-0.16
July	0.58	0.32	3.29	4.2	2.21	2.82	-0.04	-0.09

The frequency distributions of ATM observations and MISR-estimated sea ice roughness for independent test datasets for April and July are compared in Figure 2. A visual comparison of the histograms shows that April is rougher than July in our dataset and our method can effectively characterize this difference between the two seasons. These data cover a much greater spatial extent than the previous work by Nolin and Mar (2019), and R^2 is comparable to this previous work. Eventually, based on these performance metrics we selected KNN as our prediction model for our dataset.

doi:10.20944/preprints202208.0506.v1

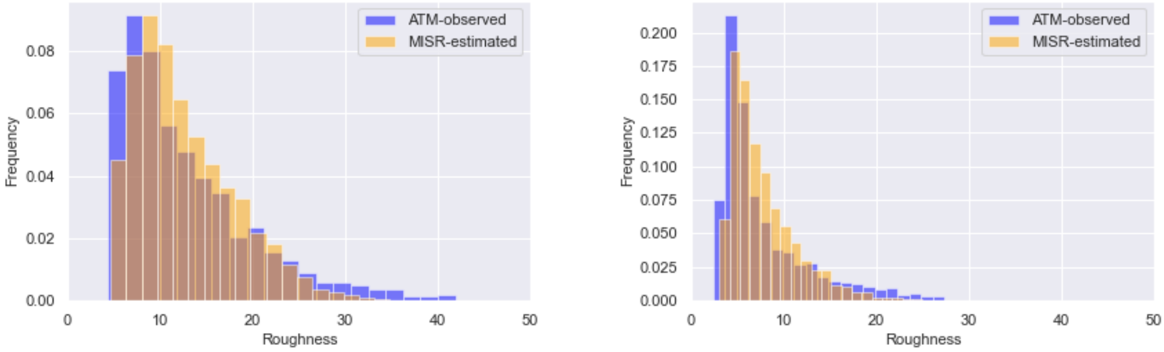

(a) (b)

Figure 2. Histograms comparing MISR-estimated (using KNN model) and ATM-observed (independent test data) sea ice roughness for (a) April and (b) July 2016.

To describe and compare the error distributions we generated quantile-quantile plots (Q–Q plots) and histograms for each month. The Q-Q plot is a scatter plot with the quantiles of the sample data (error values in our plots) on the vertical axis and the expected normal value on the horizontal axis. Q-Q visual test assumes normality and tests if residuals follow a normal distribution. If the points fall approximately along the 45-degree reference line, the two data sets come from a population with the same distribution, i.e., MISR-derived roughness values are normally distributed. Figure 3 shows the Q-Q plots that visualize roughness errors in two datasets for each month.

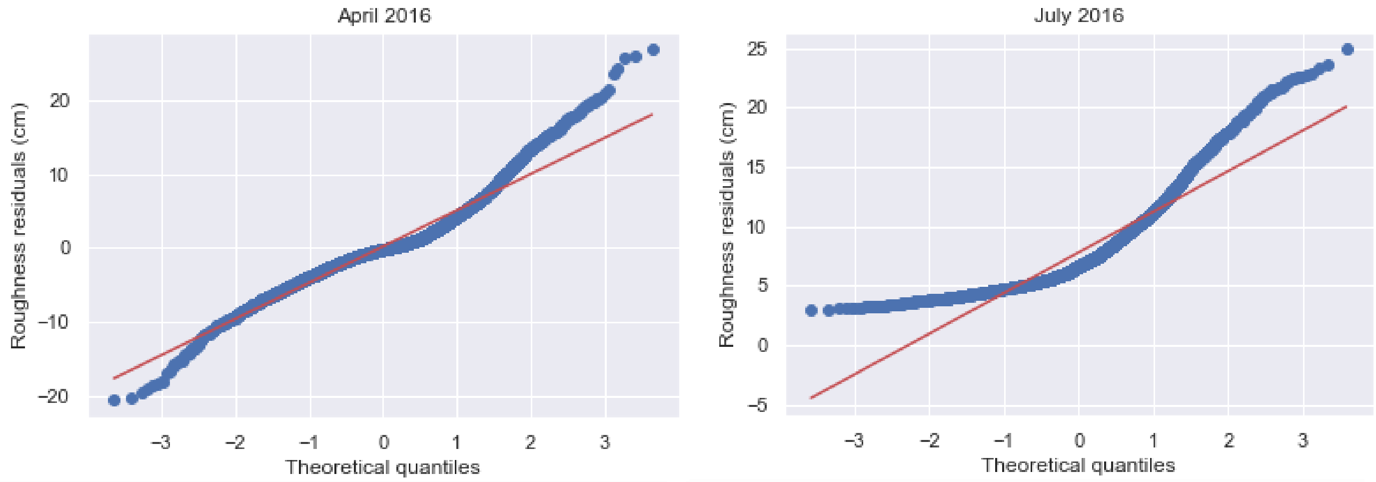

(a) (b)

Figure 3. Q-Q plots for the April and July 2016 datasets (a and b) show the error distribution of MISR-estimated roughness for (a) April and (b) July 2016.

Both Q-Q plots show deviation from the straight line, suggesting that sample residual quantiles are quite different from the theoretical quantiles and are not normally distributed. Also, both plots are skewed at their tails, but the July residual distribution is more skewed at both tails compared to the April distribution. The Q-Q plots for April (Figure 3a) show that residual points fall along the best-fit line in the middle of the graph, but the differences increase on both ends of the distribution of residuals. This indicates that residuals have more extreme values at both ends of the residual distribution. The Q-Q plots for July (Figure 3b) show a considerable deviation from the straight line on both ends of the distribution, indicating that the residuals are not normally distributed. The histograms in Figure 2 confirm that the distribution is not bell-shaped but skewed.

3.2. Spatial Patterns of Arctic Sea Ice Roughness

After evaluating the performance of the method in the previous section, we produced maps of sea ice roughness over the Arctic which included regions where ATM measurements were not available. Figure 4 shows the produced maps of sea ice roughness for April (spring) and July (summer) 2016 over the Arctic. These maps were created with the method described in section 2. Each map is produced by georeferencing every single MISR image and then creating a mosaic from all image blocks starting from block 1 to block 46 acquired in 16 days from MISR daily paths over the study area. MISR orbits repeat themselves every 16 days. Each map was created from about 9000 MISR image blocks. Overlapping blocks were averaged to create a mosaicked Arctic-wide map of mean sea ice roughness for each season. For the task of georeferencing and building the mosaic of images, we used the GDAL library.

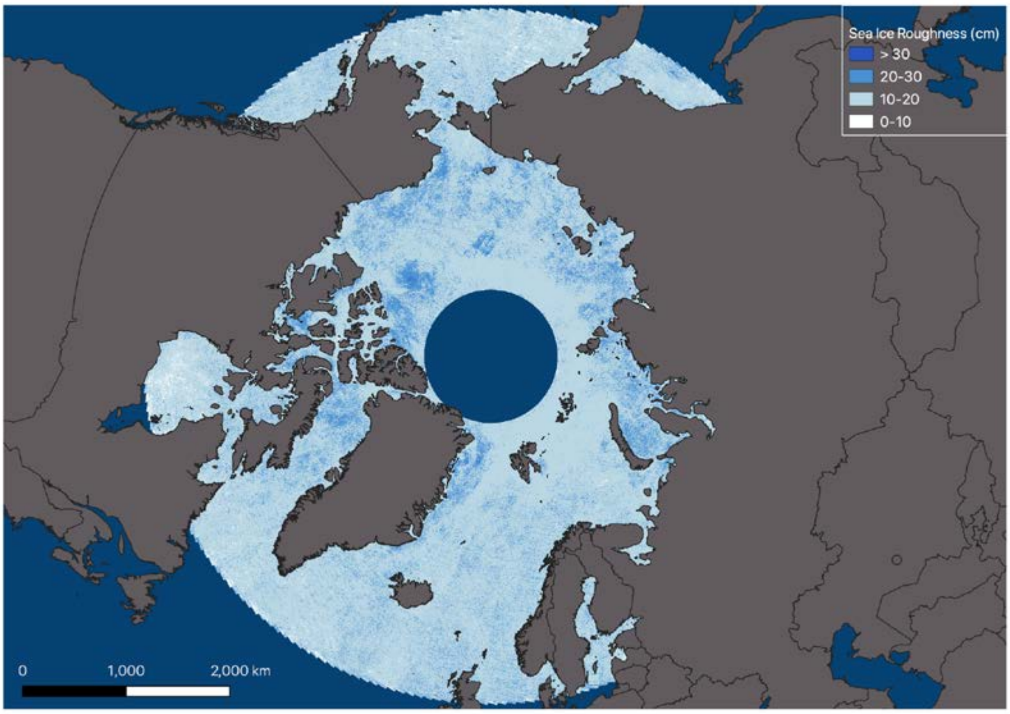

(a) April

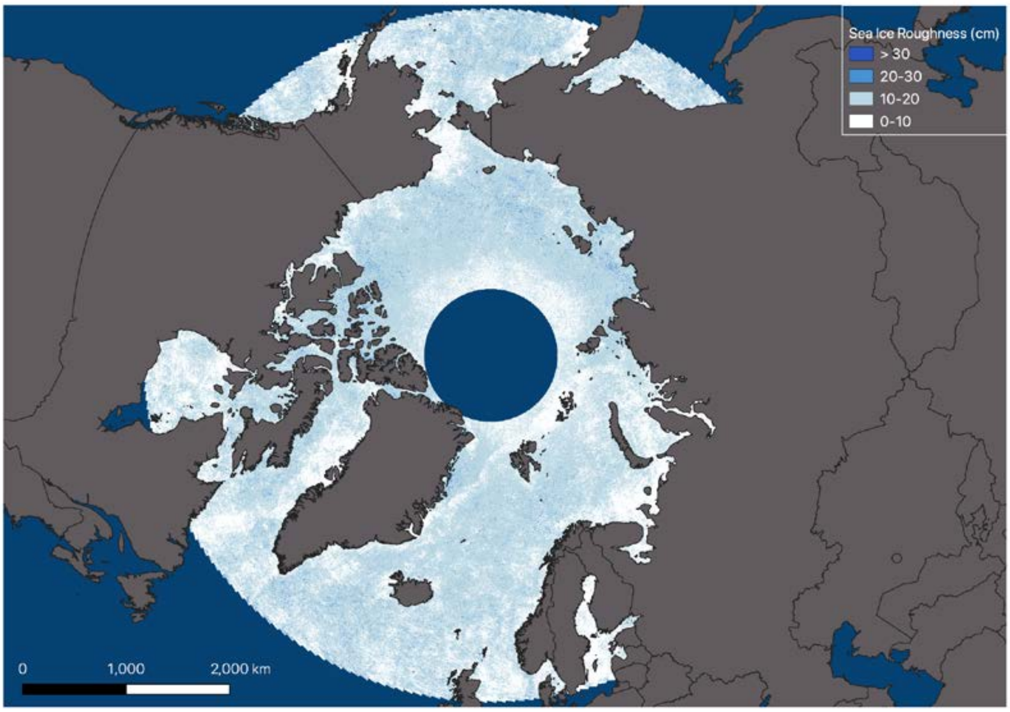

(b) July

Figure 4. Spatial patterns of mean sea ice surface roughness derived from MISR images (275 m resolution) over the Arctic region for 16-day periods of (a) 15-30 April 2016 and (b) 10-25 July 2016.

Maps in Figure 4 visualize the spatial patterns in sea ice roughness over the Arctic. They also show the temporal differences and the development of sea ice roughness averaged over the study area for the spring and summer of 2016. In the spring map, we can see that there are some rough regions where the MISR-estimated roughness values exceed 30 cm. The Arctic Ocean north of the Canadian Arctic Archipelago and Fram Strait east of Greenland are some notably rough regions in the spring map that are depicted as dark blue. Figure 5 shows these two regions in spring and summer. For instance, there is a very rough area of sea ice in the Arctic Ocean north of the Canadian Arctic Archipelago in the spring map (Figures 5a and 5b). That region usually is covered with multi-year ice [44], [45]. The roughness of multi-year ice is somewhat smooth by melt from the previous summer. Thus, this multi-year ice is maybe less rough than blocky and deformed first-year ice where ridges and deformations have not yet experienced melt.

Another rough region on the spring map is the Fram Strait (Figure 5c and 5d). This region is characterized by convergence and divergence features of sea ice and is an important gateway to exporting multiyear sea ice [46] and is one of the most dynamic regions in the Arctic Ocean especially in spring [47]. Dynamic modifications of the ice motion to the ice thickness such as ridging in that region may contribute to the thickness of sea ice and roughness patterns in that region. This suggests that the patterns of roughness in the spring map in that region could be attributed to the export of thick multiyear sea ice. Furthermore, Figure 5 shows the seasonal change of sea ice roughness from spring to summer and the decrease of sea ice roughness values in those regions. In the spring map, sea ice roughness values at the Arctic Ocean (Figure 5a) and Fram Strait (Figure 5c) are high, while the summer map shows that sea ice at the Arctic Ocean (Figure 5b) and Fram Strait (Figure 5d) have much lower roughness values. This seasonal change in sea ice roughness could be associated with the melt processes of the sea ice during the warm season [18], [19]. Summer melting reduces the thickness of the sea ice cover and contributes to the reduction of the surface roughness of sea ice.

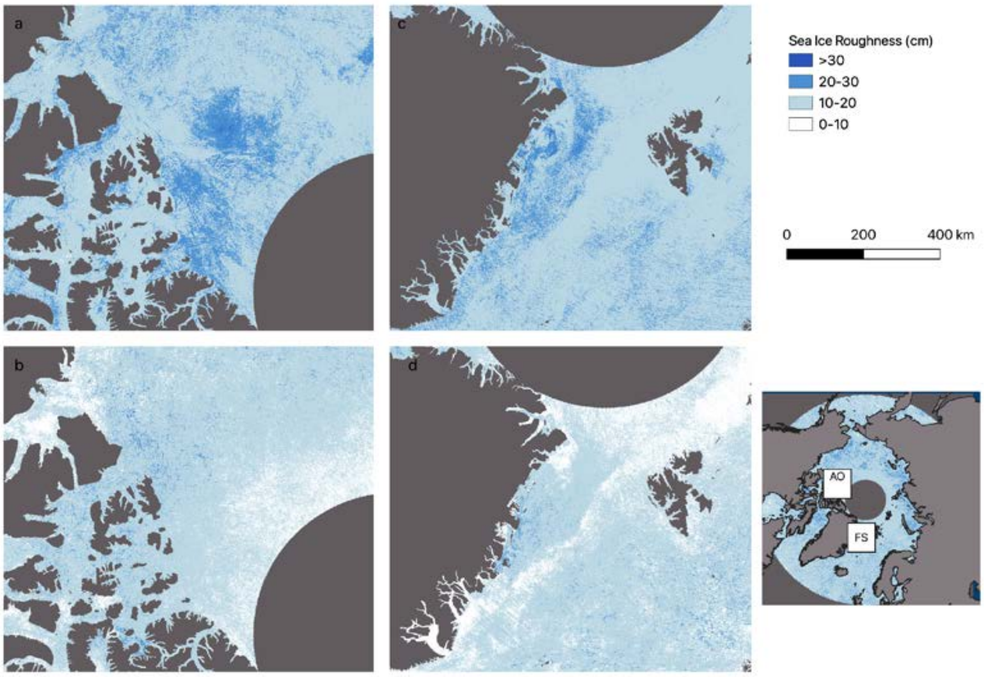

Figure 5. Mean MISR-derived sea ice surface roughness for two locations at the north of the Arctic Ocean (AO) and Fram Strait (FS): (a) the AO in spring, (b) the AO in summer, (c) FS in spring, and (d) FS in summer.

To evaluate the accuracy of our MISR-derived surface roughness maps and compare it with other remote sensing methods, we inspected two arbitrary locations and compared our MISR-derived roughness maps with Landsat 8 and Sentinel-1 images for each arbitrary region of interest. Figure 6 shows an arbitrary location at the Canadian Archipelago in April 2016. Figure 6a is our MISR-derived roughness map for an arbitrary location north of the Canadian Archipelago. Figure 6b and 6c show the same region from Landsat 8 and Sentinel-1 views, respectively. We selected and inspected zones A and B to investigate if our maps can characterize areas of land-fast ice in that region. For example, zone A and B in our roughness maps represent a smooth area. Landsat 8 image shows that zones A and B might be land-fast ice and open water. Sentinel-1 also shows zones A and B in dark color which represents a smooth surface which could be open water or land-fast ice. Also, by visually inspecting our roughness map, we drew a dashed line to separate smooth and rough surfaces of ice. One side of the dashed line is smooth ice which is represented as dark in the Sentinel-1 image and the other side that looks bright represents a rough surface. We can see that this transition from smooth to the rough surface pattern is obvious in Landsat 8 and Sentinel-1 images and our roughness map shows the same surface pattern.

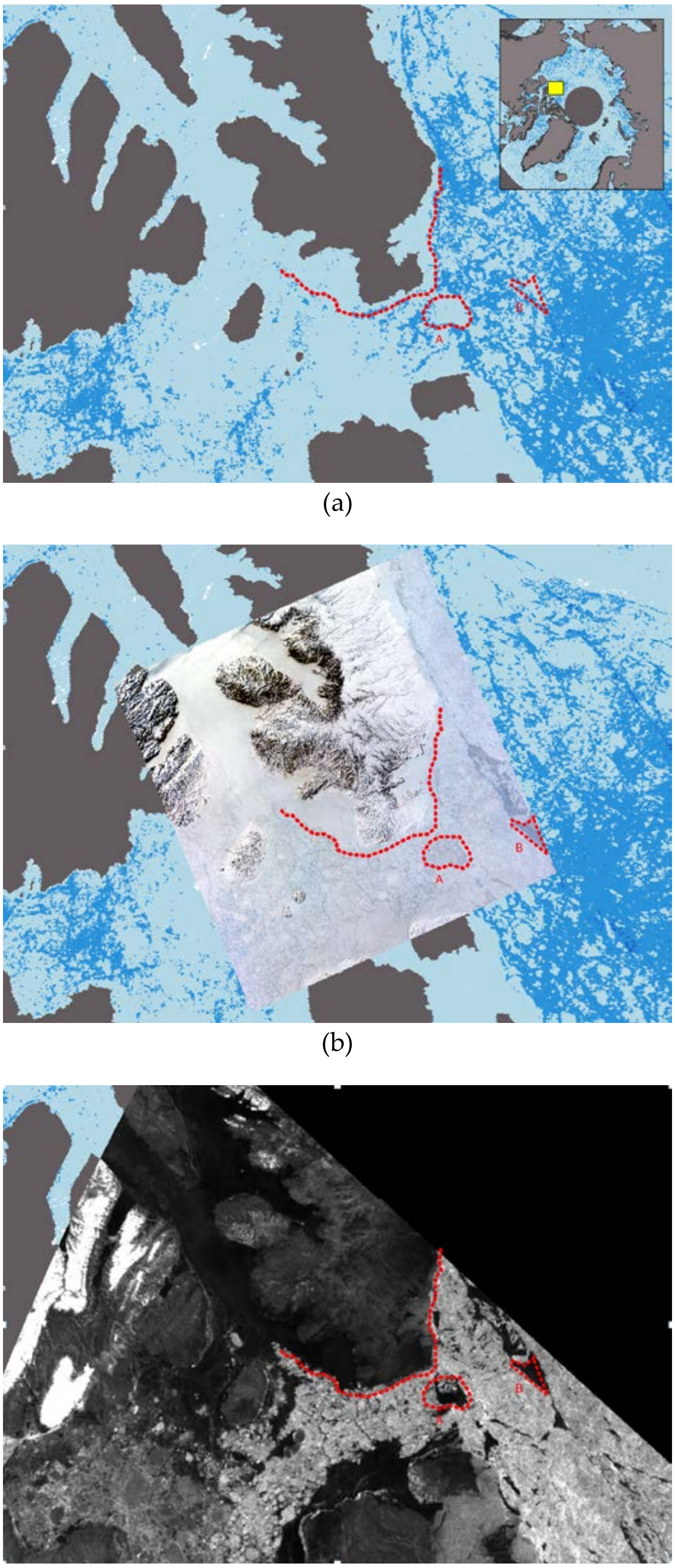

(a)

(b)

(c)

Figure 6. Comparison of (a) MISR-derived roughness map with (b) Landsat 8 and (c) Sentinel-1 images at an arbitrary location north of the Canadian Archipelago on 29 April 2016 at 116.1 W and 77.5 N.

We also inspected some areas adjacent to the east coast of Greenland in our July roughness map. Figure 7 shows an arbitrary location at the Fram Strait in July 2016.

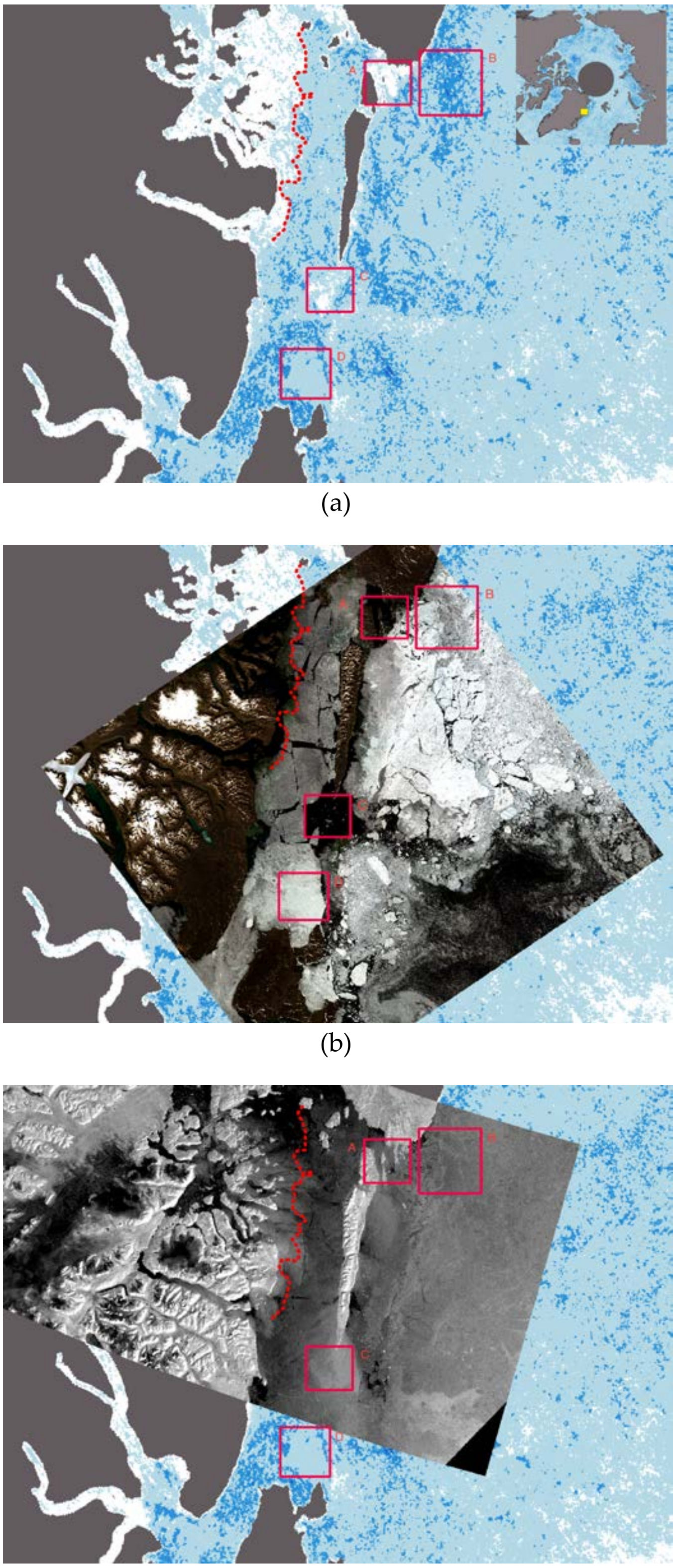

(a)

(b)

(c)

Figure 7. Comparison of (a) MISR-derived roughness map with (b) Landsat 8 for July 20th and (c) Sentinel-1 for July 19th images at an arbitrary location at the Fram Strait in July 2016 at 18.7 W and 76.5 N.

Like Figure 6, we inspected a few zones in our MISR-derived roughness map for July 2016 at Fram Strait and compared them with Landsat 8 and Sentinel-1 images for the same location. Sentinel-1 image was not available for the same location on July 20th, so we used a Sentinel-1 image for July 19th instead. In Figure 7b we can see in the Landsat 8 image that zones A and C are open water. We can see the same pattern in our roughness map and zones A and C are mapped in white and represent a smooth surface. Although the Sentinel-1 image was taken a day before the Landsat 8 image, it represents the same surface patterns. Zone D in the Landsat 8 image represents a smooth surface and our roughness map has also captured that surface pattern and mapped it as a smooth surface. Also, the Landsat 8 image shows that zone B is an example of the mixture of the smooth and rough zone. Our roughness map shows the same pattern and maps zone B in light and dark blue color which represents a mixture of smooth and rough surface patterns. The same pattern can be observed in zone B in the Sentinel-1 image.

Also, we visually inspected the Landsat 8 image and drew a dashed line and separated smooth ice and open water from rough ice. We can see in the Landsat 8 image that one side of the dashed line is open water which is represented as dark in the image and the other side includes sea ice which is represented as bright in the Landsat 8 image. In our roughness map, we can see this surface pattern clearly on both sides of the line and this transition from smooth to rough surface patterns is mapped with a transition from white to blue colored areas. Landsat 8 and Sentinel-1 images and our roughness map shows the same surface pattern. Therefore, we can conclude that our roughness maps can characterize surface patterns of smooth and rough ice.

4. Discussion and Conclusions

In this paper, we described how we developed our sea ice roughness data product. We also provided estimations of the surface roughness of sea ice by creating Arctic-wide maps of sea ice roughness for spring and summer seasons from MISR multiangular reflectance information. We showed that this appears to be a promising method for quantifying and mapping Arctic-wide sea ice surface roughness and can characterize spatial patterns and variability of sea ice surface topography and seasonal changes in sea ice roughness over an extensive area for different seasons at a horizontal scale of 275 m. The spatial patterns and their seasonal changes are consistent with other similar studies mentioned in the results section. To the best of our knowledge, this is the first attempt in creating Arctic-wide maps of sea ice roughness from MISR multiangular information.

There are several potential sources of error and uncertainty that should be taken into consideration for future improvements of this method. These include cloud detection, the number of ATM samples in a MISR pixel and their temporal co-occurrences in the training data, and challenges in distinguishing between open water and very thin smooth sea ice. Among all mentioned error sources, clouds and cloudy training data sets are likely to contribute to a significant part of the error. If clouds were present in images that were used to build the training data set, this would introduce noise to the training data set. The goal of this research was to present the capabilities of this data product and since cloud masks over sea ice tend to classify sea ice as clouds we did not use a cloud mask in this research and we left this option to the preference of the users of this data processing system. We anticipate improved cloud detection and masking capabilities in future analyses. Cloud-free MISR images were manually selected that were concurrent and co-located with the ATM data. Also, since ATM flights occurred during clear sky days, using MISR images during the same flight day of ATM implicitly suggests that that day was not cloudy. However, finding cloud-free images for a specific location in the Arctic for the purpose of studying seasonal changes remains a significant challenge.

The number of ATM samples in each MISR pixel that were used to estimate that pixel's roughness is important for the accuracy of the MISR-derived roughness. MISR pixels that have only a few ATM roughness observations were found to have a low agreement in terms between modeled roughness and ATM-measured roughness. We found that having a minimum of 10 ATM values in a MISR pixel improved the accuracy of model output when labeling MISR pixels with ATM information. We also found that the model output was improved when the MISR images used to build the training data set were selected from the same day as the ATM flight. This differed from the methodology described in Nolin and Mar (2019), who used data from +- 1 day of the ATM overflight.

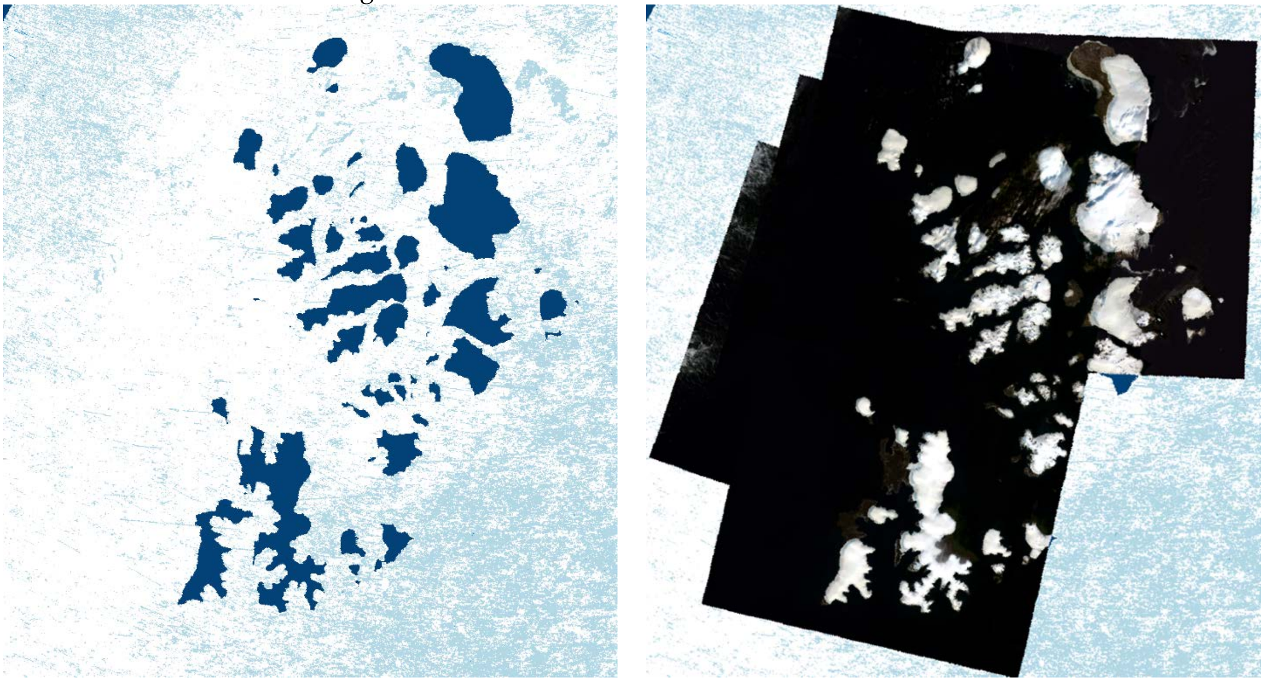
(a) (b)

Figure 8. comparison of (a) MISR-derived roughness map with (b) Landsat 8 for the ice-free area around the Zemlya George archipelago for a cloud-free period from July 10-15, 2016. Dark-blue patches in our MISR-derived map in (a) island.

At present, our model is not able to distinguish between very smooth, thin first-year sea ice (e.g., "grease ice" or "dark nilas [48] and what may be open water. We considered incorporating a reflectance threshold that could detect dark open water, but very thin first-year ice can be both smooth and dark. Thus, the July sea ice roughness maps are likely to include open water as well as sea ice. For instance, subjective visual examination of a Landsat 8 reflectance image shows that pixels mapped as 0-10 cm surface roughness appear to be ice-free. Figure 8 shows the ice-free area around the Zemlya George archipelago for a cloud-free period from July 10-15, 2016. The MISR-derived roughness map for the period July 10-25, 2016 shows this same area as having a roughness of 0-10 cm.

The histogram in Figure 2b which compares July ATM and MISR-derived sea ice roughness, shows that our model underestimates the frequency of sea ice roughness values less than about 5 cm. While the difference in spatial resolution between MISR and the ATM roughness product (275 m vs. 80 m) is likely responsible for the undercount of smooth ice, it may also be the case that some parts of the MISR pixel are smooth ice and other parts are open water.

There are strengths and limitations to any remote sensing technique. MISR data has several advantages such as a long record of data (2000-present), near-global coverage, and spatial resolution down to 250 m. Especially the broad angular coverage which is independent of its spectral coverage makes it a unique source of information. However, building data models from MISR multiangular information reveals some of its limitations that must be taken into consideration such as it requires lidar data for calibration and if the study region is over the Arctic, images tend to be cloudy and dark. To understand the full benefit, this data product still requires additional interpretation by sea ice researchers. Also, this data product can be a helpful complement to other remote sensing techniques such as ICESat-2, SAR, and high-resolution optical data. Given the quality of the MISR imagery, MISR-estimated roughness is best used for understanding the spatial patterns of sea ice roughness as well as the detailed daily estimates of sea ice roughness. Also, averaged Arctic-wide maps are more useful for understanding and diagnosing the changing patterns of mean sea ice roughness in seasonal and long-term studies of sea ice roughness in the Arctic. Therefore, considering that sea ice roughness can serve as a proxy for other sea ice characteristics such as thickness and age, this data product can be beneficial to improving our understanding of the roughness patterns over the Arctic region and can be a helpful tool for the Arctic science community.

Author Contributions: Conceptualization, A.N. and E.M.; methodology, A.N. and E.M.; software, E.M.; validation, E.M.; formal analysis, E.M.; investigation, E.M.; resources, A.N.; data curation, E.M.; writing—original draft preparation, E.M.; writing—review and editing, A.N.; visualization, E.M.; supervision, A.N.; project administration, A.N.; funding acquisition, A.N.

Funding: This research was funded on a subcontract (#1623719) through the MISR Project, NASA/Jet Propulsion Laboratory.

Data Availability Statement: Code and data are publicly available from the following repositories and websites: GitHub page for sea ice roughness information and scripts is available online at https://github.com/misrrepo/MISR-SeaIceRoughness.

Acknowledgments: These data were obtained from the NASA Langley Research Center Atmospheric Science Data Center.

Conflicts of Interest: The authors declare no conflict of interest.

References

[1] Rantanen, M.; Karpechko, A. Y.; Lipponen, A.; Nordling, K.; Hyvärinen, O.; Ruosteenoja, K.; Vihma, T.; Laaksonen, A. The Arctic Has Warmed Nearly Four Times Faster than the Globe since 1979. *Commun. Earth Environ.* **2022**, *3* (1), 1–10. https://doi.org/10.1038/s43247-022-00498-3.

[2] Holland, M. M.; Bitz, C. M.; Tremblay, B. Future Abrupt Reductions in the Summer Arctic Sea Ice. *Geophys. Res. Lett.* **2006**, *33* (23). https://doi.org/10.1029/2006GL028024.

[3] Kumar, A.; Yadav, J.; Mohan, R. Global Warming Leading to Alarming Recession of the Arctic Sea-Ice Cover: Insights from Remote Sensing Observations and Model Reanalysis. *Heliyon* **2020**, *6* (7), e04355. https://doi.org/10.1016/j.heliyon.2020.e04355.

[4] Meier, W. N.; Hovelsrud, G. K.; van Oort, B. E. H.; Key, J. R.; Kovacs, K. M.; Michel, C.; Haas, C.; Granskog, M. A.; Gerland, S.; Perovich, D. K.; Makshtas, A.; Reist, J. D. Arctic Sea Ice in Transformation: A Review of Recent Observed Changes and Impacts on Biology and Human Activity. *Rev. Geophys.* **2014**, *52* (3), 185–217. https://doi.org/10.1002/2013RG000431.

[5] Mueller, B. L.; Gillett, N. P.; Monahan, A. H.; Zwiers, F. W. Attribution of Arctic Sea Ice Decline from 1953 to 2012 to Influences from Natural, Greenhouse Gas, and Anthropogenic Aerosol Forcing. *J. Clim.* **2018**, *31* (19), 7771–7787. https://doi.org/10.1175/JCLI-D-17-0552.1.

[6] Notz, D.; Community, S. Arctic Sea Ice in CMIP6. *Geophys. Res. Lett.* **2020**, *47* (10), e2019GL086749. https://doi.org/10.1029/2019GL086749.

[7] Stroeve, J.; Notz, D. Insights on Past and Future Sea-Ice Evolution from Combining Observations and Models. *Glob. Planet. Change* **2015**, *135*, 119–132. https://doi.org/10.1016/j.gloplacha.2015.10.011.

[8] Kwok, R.; Rothrock, D. A. Decline in Arctic Sea Ice Thickness from Submarine and ICESat Records: 1958–2008. *Geophys. Res. Lett.* **2009**, *36* (15). https://doi.org/10.1029/2009GL039035.

[9] Meier, W. N.; Stroeve, J.; Fetterer, F. Whither Arctic Sea Ice? A Clear Signal of Decline Regionally, Seasonally and Extending beyond the Satellite Record. *Ann. Glaciol.* **2007**, *46*, 428–434. https://doi.org/10.3189/172756407782871170.

[10] Stroeve, J.; Notz, D. Changing State of Arctic Sea Ice across All Seasons. *Environ. Res. Lett.* **2018**, *13* (10), 103001. https://doi.org/10.1088/1748-9326/aade56.

[11] Cavalieri, D. J.; Parkinson, C. L.; Gloersen, P.; Comiso, J. C.; Zwally, H. J. Deriving Long-Term Time Series of Sea Ice Cover from Satellite Passive-Microwave Multisensor Data Sets. *J. Geophys. Res. Oceans* **1999**, *104* (C7), 15803–15814. https://doi.org/10.1029/1999JC900081.

[12] Comiso, J. C. A Rapidly Declining Perennial Sea Ice Cover in the Arctic. *Geophys. Res. Lett.* **2002**, *29* (20), 17-1-17–4. https://doi.org/10.1029/2002GL015650.

[13] Comiso, J. C.; Parkinson, C. L.; Gersten, R.; Stock, L. Accelerated Decline in the Arctic Sea Ice Cover. *Geophys. Res. Lett.* **2008**, *35* (1). https://doi.org/10.1029/2007GL031972.

[14] Parkinson, C. L.; Cavalieri, D. J.; Gloersen, P.; Zwally, H. J.; Comiso, J. C. Arctic Sea Ice Extents, Areas, and Trends, 1978–1996. *J. Geophys. Res. Oceans* **1999**, *104* (C9), 20837–20856. https://doi.org/10.1029/1999JC900082.

[15] Serreze, M. C.; Maslanik, J. A.; Scambos, T. A.; Fetterer, F.; Stroeve, J.; Knowles, K.; Fowler, C.; Drobot, S.; Barry, R. G.; Haran, T. M. A Record Minimum Arctic Sea Ice Extent and Area in 2002. *Geophys. Res. Lett.* **2003**, *30* (3). https://doi.org/10.1029/2002GL016406.

[16] Farrell, S. L.; Duncan, K.; Buckley, E. M.; Richter-Menge, J.; Li, R. Mapping Sea Ice Surface Topography in High Fidelity With ICESat-2. *Geophys. Res. Lett.* **2020**, *47* (21), e2020GL090708. https://doi.org/10.1029/2020GL090708.

[17] Kharbouche, S.; Muller, J.-P. Sea Ice Albedo from MISR and MODIS: Production, Validation, and Trend Analysis. *Remote Sens.* **2019**, *11* (1), 9. https://doi.org/10.3390/rs11010009.

[18] Kwok, R.; Cunningham, G. F.; Wensnahan, M.; Rigor, I.; Zwally, H. J.; Yi, D. Thinning and Volume Loss of the Arctic Ocean Sea Ice Cover: 2003–2008. *J. Geophys. Res. Oceans* **2009**, *114* (C7). https://doi.org/10.1029/2009JC005312.

[19] Landy, J. C.; Ehn, J. K.; Barber, D. G. Albedo Feedback Enhanced by Smoother Arctic Sea Ice. *Geophys. Res. Lett.* **2015**, *42* (24), 10,714-10,720. https://doi.org/10.1002/2015GL066712.

[20] Yi, D.; Zwally, H. J.; Sun, X. ICESat Measurement of Greenland Ice Sheet Surface Slope and Roughness. *Ann. Glaciol.* **2005**, *42*, 83–89. https://doi.org/10.3189/172756405781812691.

[21] Segal, R. A.; Scharien, R. K.; Cafarella, S.; Tedstone, A. Characterizing Winter Landfast Sea-Ice Surface Roughness in the Canadian Arctic Archipelago Using Sentinel-1 Synthetic Aperture Radar and the Multi-Angle Imaging SpectroRadiometer. *Ann. Glaciol.* **2020**, *61* (83), 284–298. https://doi.org/10.1017/aog.2020.48.

[22] Andreas, E. L.; Horst, T. W.; Grachev, A. A.; Persson, P. O. G.; Fairall, C. W.; Guest, P. S.; Jordan, R. E. Parametrizing Turbulent Exchange over Summer Sea Ice and the Marginal Ice Zone. *Q. J. R. Meteorol. Soc.* **2010**, *136* (649), 927–943. https://doi.org/10.1002/qj.618.

[23] Arya, S. Contribution of Form Drag on Pressure Ridges to the Air Stress on Arctic Ice. **1973**. https://doi.org/10.1029/JC078I030P07092.

[24] Petty, A. A.; Tsamados, M. C.; Kurtz, N. T. Atmospheric Form Drag Coefficients over Arctic Sea Ice Using Remotely Sensed Ice Topography Data, Spring 2009-2015: ATMOSPHERIC DRAG OVER ARCTIC SEA ICE. *J. Geophys. Res. Earth Surf.* **2017**, *122* (8), 1472–1490. https://doi.org/10.1002/2017JF004209.

[25] Steiner, N.; Harder, M.; Lemke, P. Sea-Ice Roughness and Drag Coefficients in a Dynamic–Thermodynamic Sea-Ice Model for the Arctic. *Tellus Dyn. Meteorol. Oceanogr.* **1999**, *51* (5), 964–978. https://doi.org/10.3402/tellusa.v51i5.14505.

[26] Arya, S. P. S. A Drag Partition Theory for Determining the Large-Scale Roughness Parameter and Wind Stress on the Arctic Pack Ice. *J. Geophys. Res. 1896-1977* **1975**, *80* (24), 3447–3454. https://doi.org/10.1029/JC080i024p03447.

[27] Castellani, G.; Lüpkes, C.; Hendricks, S.; Gerdes, R. Variability of Arctic Sea-Ice Topography and Its Impact on the Atmospheric Surface Drag. *J. Geophys. Res. Oceans* **2014**, *119* (10), 6743–6762. https://doi.org/10.1002/2013JC009712.

[28] Guest, P. S.; Davidson, K. L. The Aerodynamic Roughness of Different Types of Sea Ice. *J. Geophys. Res. Oceans* **1991**, *96* (C3), 4709–4721. https://doi.org/10.1029/90JC02261.

[29] Lüpkes, C.; Gryanik, V. M.; Rösel, A.; Birnbaum, G.; Kaleschke, L. Effect of Sea Ice Morphology during Arctic Summer on Atmospheric Drag Coefficients Used in Climate Models. *Geophys. Res. Lett.* **2013**, *40* (2), 446–451. https://doi.org/10.1002/grl.50081.

[30] Lüpkes, C.; Gryanik, V. M.; Hartmann, J.; Andreas, E. L. A Parametrization, Based on Sea Ice Morphology, of the Neutral Atmospheric Drag Coefficients for Weather Prediction and Climate Models. *J. Geophys. Res. Atmospheres* **2012**, *117* (D13). https://doi.org/10.1029/2012JD017630.

[31] Lei, R.; Tian-Kunze, X.; Leppäranta, M.; Wang, J.; Kaleschke, L.; Zhang, Z. Changes in Summer Sea Ice, Albedo, and Portioning of Surface Solar Radiation in the Pacific Sector of Arctic Ocean during 1982–2009. *J. Geophys. Res. Oceans* **2016**, *121* (8), 5470–5486. https://doi.org/10.1002/2016JC011831.

[32] Lindsay, R. W.; Zhang, J. The Thinning of Arctic Sea Ice, 1988–2003: Have We Passed a Tipping Point? *J. Clim.* **2005**, *18* (22), 4879–4894. https://doi.org/10.1175/JCLI3587.1.

[33] Moritz, R. E.; Bitz, C. M.; Steig, E. J. Dynamics of Recent Climate Change in the Arctic. *Science* **2002**, *297* (5586), 1497–1502. https://doi.org/10.1126/science.1076522.

[34] Perovich, D. K.; Polashenski, C. Albedo Evolution of Seasonal Arctic Sea Ice: ALEDO EVOLUTION OF SEASONAL SEA ICE. *Geophys. Res. Lett.* **2012**, *39* (8), n/a-n/a. https://doi.org/10.1029/2012GL051432.

[35] Stroeve, J. C.; Kattsov, V.; Barrett, A.; Serreze, M.; Pavlova, T.; Holland, M.; Meier, W. N. Trends in Arctic Sea Ice Extent from CMIP5, CMIP3 and Observations. *Geophys. Res. Lett.* **2012**, *39* (16). https://doi.org/10.1029/2012GL052676.

[36] Zhang, J.; Rothrock, D.; Steele, M. Recent Changes in Arctic Sea Ice: The Interplay between Ice Dynamics and Thermodynamics. *J. Clim.* **2000**, *13* (17), 3099–3114. https://doi.org/10.1175/1520-0442(2000)013<3099:RCIASI>2.0.CO;2.

[37] Nolin, A. W.; Mar, E. Arctic Sea Ice Surface Roughness Estimated from Multi-Angular Reflectance Satellite Imagery. *Remote Sens.* **2019**, *11* (1), 50. https://doi.org/10.3390/rs11010050.

[38] Nolin, A. W.; Fetterer, F. M.; Scambos, T. A. Surface Roughness Characterizations of Sea Ice and Ice Sheets: Case Studies with MISR Data. *IEEE Trans. Geosci. Remote Sens.* **2002**, *40* (7), 1605–1615. https://doi.org/10.1109/TGRS.2002.801581.

[39] Diner, D. J.; Asner, G. P.; Davies, R.; Knyazikhin, Y.; Muller, J.-P.; Nolin, A. W.; Pinty, B.; Schaaf, C. B.; Stroeve, J. New Directions in Earth Observing: Scientific Applications of Multiangle Remote Sensing. *Bull. Am. Meteorol. Soc.* **1999**, *80* (11), 2209–2228. https://doi.org/10.1175/1520-0477(1999)080<2209:NDIEOS>2.0.CO;2.

[40] Nolin, A. W. Towards Retrieval of Forest Cover Density over Snow from the Multi-Angle Imaging SpectroRadiometer (MISR). *Hydrol. Process.* **2004**, *18* (18), 3623–3636. https://doi.org/10.1002/hyp.5803.

[41] Diner, D. J.; Beckert, J. C.; Reilly, T. H.; Bruegge, C. J.; Conel, J. E.; Kahn, R. A.; Martonchik, J. V.; Ackerman, T. P.; Davies, R.; Gerstl, S. A. W.; Gordon, H. R.; Muller, J.-P.; Myneni, R. B.; Sellers, P. J.; Pinty, B.; Verstraete, M. M. Multi-Angle Imaging SpectroRadiometer (MISR) Instrument Description and Experiment Overview. *IEEE Trans. Geosci. Remote Sens.* **1998**, *36* (4), *1072–1087. https://doi.org/10.1109/36.700992.*

[42] Studinger, M. 2014, updated 2020. IceBridge ATM L2 Icessn Elevation, Slope, and Roughness, Version 2. Boulder, Colorado USA. NASA National Snow and Ice Data Center Distributed Active Archive Center. https://doi.org/10.5067/CPRXXK3F39RV. [Last Accessed 21 August 2022].

[43] Brunt, K. M.; Hawley, R. L.; Lutz, E. R.; Studinger, M.; Sonntag, J. G.; Hofton, M. A.; Andrews, L. C.; Neumann, T. A. Assessment of NASA Airborne Laser Altimetry Data Using Ground-Based GPS Data near Summit Station, Greenland. *The Cryosphere* **2017**, *11* (2), 681–692. https://doi.org/10.5194/tc-11-681-2017.

[44] Kwok, R.; Kacimi, S.; Webster, M. a.; Kurtz, N. t.; Petty, A. a. Arctic Snow Depth and Sea Ice Thickness From ICESat-2 and CryoSat-2 Freeboards: A First Examination. *J. Geophys. Res. Oceans* **2020**, *125* (3), e2019JC016008. https://doi.org/10.1029/2019JC016008.

[45] Kwok, R.; Cunningham, G. F. Variability of Arctic Sea Ice Thickness and Volume from CryoSat-2. *Philos. Trans. R. Soc. Math. Phys. Eng. Sci.* **2015**, *373* (2045), 20140157. https://doi.org/10.1098/rsta.2014.0157.

[46] Kwok, R.; Schweiger, A.; Rothrock, D. A.; Pang, S.; Kottmeier, C. Sea Ice Motion from Satellite Passive Microwave Imagery Assessed with ERS SAR and Buoy Motions. *J. Geophys. Res. Oceans* **1998**, *103* (C4), 8191–8214. https://doi.org/10.1029/97JC03334.

[47] Min, C.; Mu, L.; Yang, Q.; Ricker, R.; Shi, Q.; Han, B.; Wu, R.; Liu, J. Sea Ice Export through the Fram Strait Derived from a Combined Model and Satellite Data Set. *The Cryosphere* **2019**, *13* (12), 3209–3224. https://doi.org/10.5194/tc-13-3209-2019.

[48] Sea Ice Glossary - Woods Hole Oceanographic Institution. Available online: *https://www.whoi.edu/.* (accessed on 25 August 2022).